

A 3D-printed device for in situ monitoring of an organic redox-flow battery via NMR/MRI

Borja Caja-Munoz, Kévin Chighine, Jean-Pierre Dognon, Lionel Dubois, Patrick Berthault

▶ **To cite this version:**

Borja Caja-Munoz, Kévin Chighine, Jean-Pierre Dognon, Lionel Dubois, Patrick Berthault. A 3D-printed device for in situ monitoring of an organic redox-flow battery via NMR/MRI. Analytical Chemistry, 2023, 95 (14), pp.6020-6028. 10.1021/acs.analchem.3c00051 . cea-04065111

HAL Id: cea-04065111
https://cea.hal.science/cea-04065111

Submitted on 11 Apr 2023

HAL is a multi-disciplinary open access archive for the deposit and dissemination of scientific research documents, whether they are published or not. The documents may come from teaching and research institutions in France or abroad, or from public or private research centers.

L'archive ouverte pluridisciplinaire **HAL**, est destinée au dépôt et à la diffusion de documents scientifiques de niveau recherche, publiés ou non, émanant des établissements d'enseignement et de recherche français ou étrangers, des laboratoires publics ou privés.

A 3D-printed device for in situ monitoring of an organic redox-flow battery via NMR/MRI

Borja Caja-Munoz,‡ Kévin Chighine,‡ Jean-Pierre Dognon,‡ Lionel Dubois,§ and Patrick Berthault*,‡

‡ NIMBE, CEA, CNRS, Université de Paris Saclay, CEA Saclay, 91191 Gif-sur-Yvette, France

§ Univ. Grenoble Alpes, CEA, CNRS, IRIG-SyMMES UMR 5819, 38000 Grenoble, France

KEYWORDS: Battery, Redox-flow, NMR, MRI, Operando, 3D printing, Anthraquinone

ABSTRACT: A mini organic redox-flow battery pluggable on the basis of a high-resolution NMR probehead has been conceived and built mainly by 3D printing. This device allows the realization of all modern spectroscopy experiments as well as imaging experiments. It has been tested for the real-time monitoring of redox cycling of 9,10-Anthraquinone-2,7-disulfonic acid disodium salt (2,7-AQDS) in acidic conditions, which has revealed the preponderant role of dimerization in the processes of oxidation and reduction. Determination of the thermodynamic properties of homo- and heterodimer formation through quantum chemical, multilevel modeling workflows confirm our hypotheses about the molecular processes occurring during charge and discharge.

Large-scale development of renewable intermittent energy has led to a strong increase in storage capacity needs. As it allows dissociating quantity of store energy and power, redox-flow batteries (RFB) are specifically suited and developed for the large-scale stationary energy storage. In this technology, two electrolytes, able to exchange electrical charges at low (negolyte) or high (posolyte) potential, are pumped from the tank where they are stored through a conversion cell where the electrochemical process takes place. Nowadays, vanadium redox-flow battery (V-RFB) is the most developed and used RFB technology. Due to the cost and scarcity of vanadium, new chemistries based on organic redox molecules (O-RFB) are in development, mainly based on quinone chemistry. However, the high molecular concentration in solution (up to 2 or 3 M) giving rise to a lot of side reactions, associated or not to electron transfer during cycling, can result in a rapid loss of performances. For example, dimerization / polymerization or chemical modification can lead to a complete degradation of the electrolyte properties.[1,2]

As a consequence, there is strong need to develop operando analysis tools to understand degradation processes occurring during O-RFB cycling. Strongly linked to the electrochemical process, self-diffusion of the species near the electrodes is also a very important parameter to study in order to understand O-RFB performance degradations. In such a field, NMR is a powerful tool, as this non-destructive modality enables a detailed analysis at the atomic scale allowing studies of both chemical structure of organic molecule and diffusion process associated to each species in solution. The usual method would consist in manually sample the electrolyte solution during battery operation and fill NMR tubes for high resolution analysis. The problem with such an approach is that it requires opening the electrolyte reservoir, which can introduce air in the circuit, leading to unwanted oxidation of the generated chemical species. Since the first in situ spectroscopic study of an electrochemical cell in 1964[3] until recently,[4] several approaches have been developed in order to identifying species electrochemically generated in solution. In the case of electrochemistry-NMR coupling some studies[5,6,7] utilized a flow cell arrangement in which the electrochemical reaction takes place outside of the radio frequency coils of the probe

and the product was subsequently flowed into the detection area. These setups provide suitable conditions for the NMR measurements (enhanced field homogeneity) and allow the coupling with other spectroscopic methods such as EPR.[8] Nevertheless, they require large solution volumes and, above all, there is an inherent time delay between formation and detection of products and intermediates (leading to an indirect, non-real-time, monitoring method). As some products are not stable over time, other research groups decided to perform EC-NMR studies in a three-electrode mode with the working electrode positioned inside the NMR-active region ("probe-in"), simultaneously generating and detecting the electrochemical products (for a recent review on the analysis tools of electrochemical processes, see ref. 9).

Here we present a device for the operando NMR monitoring of a mini-organic redox-flow battery that exhibits several advantages. First, being in large part built by 3D-printing, it is of reduced size and can fit inside a narrow-bore magnet of a high-resolution NMR spectrometer. Its size is also an advantage for the quantity of organic redox derivatives that one might want to test but which price could be elevated. Second, it is designed to be electrically plugged onto the basis of a Bruker Micro-5 imaging probe, for the radiofrequency tuning/matching. This imposes a maximum diameter of 18 mm, but in this way, both magnetic resonance imaging and localized spectroscopy experiments can be achieved with the commercial hardware and software. For the circulation of the electrolyte we capitalize on the principle of the mini bubble pump that we developed a few years ago, for applications ranging from dissolution of hyperpolarized species,[10] to study of slowly relaxing nuclei.[11,12] A flow of inert gas drives the motion of the electrolyte solution in the circuit shown in Figure 1, so that the molecules at the working electrode surface are constantly renewed. This operando device is tested on 9,10-anthraquinone-2,7-disulfonic acid disodium salt (2,7-AQDS) in acidic conditions, which behaviour in redox-flow devices is well documented.[13,14]

For the purpose of the study of the evolution of the 2,7-AQDS molecules during charge and discharge cycles, the compartment of the counter-electrode contains only the solvent in the same concentration as in the main reservoir. The design of the mini-organic redox-flow battery (see Figure 1, and the full-size version in Figure S1 of the Supporting Information) is optimized according to the following specifications: i) a large volume is devoted to the NMR detection area which is centred with respect to the magnet bore (region of highest static field homogeneity) and is flanked by saddle coils in order to exhibit a high filling factor; ii) the bubbles that create the solution flow must not reach either the NMR detection area or the membrane region; iii) the working electrode – counter electrode distance is optimized in order to minimize the ohmic drop of the cell; iv) the geometry of the cell is such that the diffusion of the ions is as much as possible parallel to the static magnetic field, which minimizes the magneto-hydrodynamic effect.[15,16] It is still present, but low enough that it does not significantly modify the behaviour of the battery (see below).

The CAD of the battery was made in three parts fitted together. This not only facilitates the cleaning of crevices after Polyjet 3D printing, but also allows the insertion of aluminium foils horizontally on either side of the middle piece to act as rf insulators. The material chosen for printing is PMMA, not solely to provide transparent parts, but also because its magnetic susceptibility is close to that of water, thus of the study medium. The bottom part (1) is devoted to the connection to the NMR probe basis; it contains the inductors and capacitors. The channel constituting the loop of the solution circuit is also in this part. The middle part (2) contains the rising and falling parts of the solution channels, the latter being surrounded by saddle coils while the former is isolated by winding of an aluminium foil. We denote this region as the NMR area. Two other aluminium foils are placed horizontally between parts (1) and (2) and (2) and (3). Without this rf isolation the entire solution circuit loop, including the rising portion of the solution channel and the upper tank, is detected, as displayed in Figure S2.

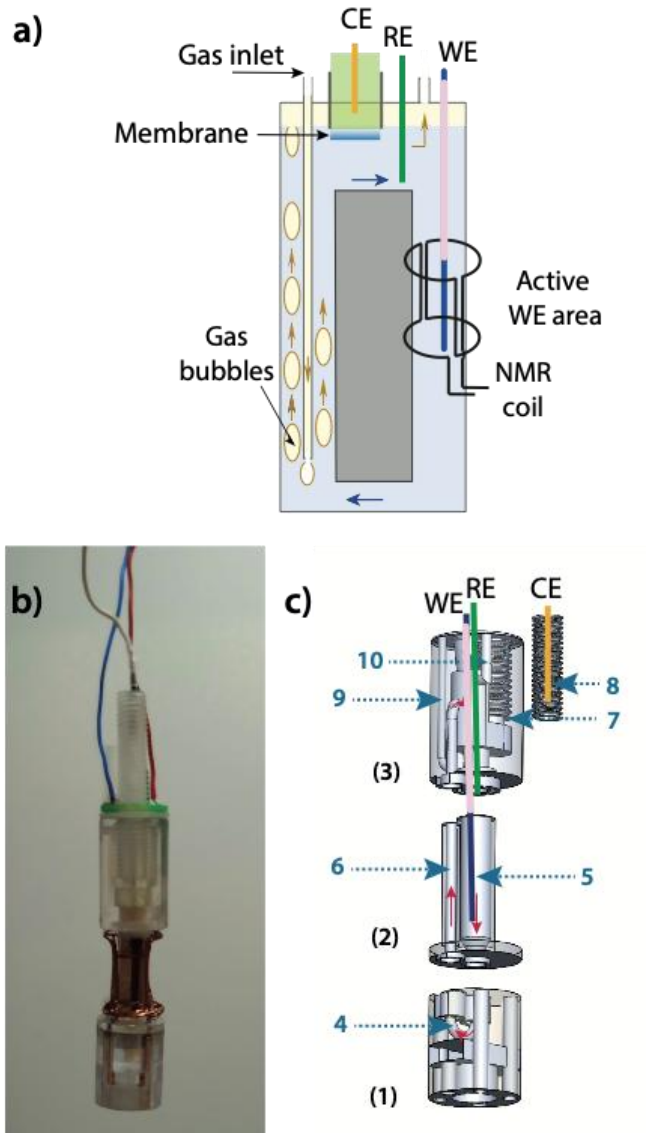


Figure 1. The mini redox-flow battery. a) Schematic diagram. WE: working electrode; RE: reference electrode; CE: counter-electrode. b) Picture; c) 3D rendering of the bottom (1), middle (2) and top (3) parts of the device. (4) Solution circuit loop, (5) NMR area, (6) back channel, rf-isolated with aluminum foil, (7) proton-exchange membrane, (8) counter-electrode compartment, (9) nitrogen inlet, (10) nitrogen exhaust, WE: working electrode (glassy carbon), RE: reference electrode (Ag/AgCl), CE: counter-electrode (Pt). For the sake of clarity, neither the rf coils nor the copper connectors at the bottom of the part (1) for the electric connection to the NMR probehead are drawn.

The top part (3) is the most complex. i) The 3D printing of a cylindrical receptacle bordered by a screw thread allows to receive the Nafion membrane and the tank containing the counter-electrode. This part is axially offset to leave room for the working and reference electrodes. The upper part of the working electrode, outside the NMR detection area, is insulated by a heat-shrinkable sheath. ii) The gas inlet is high enough in the part to avoid the formation of bubbles at the membrane surface. iii) The gas outlet is far enough from the inlet enabling high-speed bubbling to put into circulation the electrolyte solution, while avoiding it from pouring out of the insert. On top of this part a PCB (print card board) on which the reference electrode and the working electrode are welted achieves the interface with the potentiostat

connectors. Between the PCB and the 3D printed piece, a cut sized silicon foil renders the latter gas proof, in order to avoid any unwanted oxidation. The fully dimensioned drawings of the cell are provided in the Supporting Information (Figs. S3-S6).

The proof of concept of the performances of this device have been made on a spectrometer working at 11.7 T (^{1}H Larmor frequency 500 MHz). Several versions of this disposable insert have been printed and equipped with either a single ^{1}H saddle coil or two ^{1}H and ^{13}C saddle coils in quadrature, in direct (inner coil ^{13}C) or inverse mode (inner coil ^{1}H). The experiments which are now described have been performed in this configuration. In a first time, field homogeneity has been optimized, in particular thanks to B_0 mapping. ^{1}H and ^{13}C pulses have been calibrated. Then 2D ^{1}H gradient echo imaging experiments have been performed to set up the localized spectroscopy experiments inside the NMR reservoir. Figure 2a displays such longitudinal and axial images recorded with the electrode in place. The donut shape of the axial image is due to the presence of the electrode. The images reveal that the aluminium foils act as expected: only the area of interest (5) in Figure 1c gives an NMR signal. Such images enable us to select a pixel of interest outside the electrode region for a ^{1}H spectrum with high resolution through PRESS or STEAM approaches (Figure 2b). On the spectrum localized in the 2.4 mm x 2.4 mm region delimited by the red dashed line, a resolution better than 4 Hz is achieved, and the J_{HH} scalar couplings are well observed. The water signal also is not too broad, and the anthraquinone signals can be observed without pre-saturation. It is be possible to improve this spectral resolution, by taking a smaller voxel, but obviously at the cost of a lower signal-to-noise ratio per time unit. A compromise allowing to obtain a spectral resolution not too degraded while keeping enough signal to monitor the battery in action is here chosen. The 13C spectrum (recorded without spatial localization) shows as expected the signals of the oxidized form of the anthraquinone, see Fig. 2c. Note that the 1H-decoupling is efficient.

The identification of the redox state of the 2,7-AQDS is thus possible at any state of charge of the battery. The only limitation is link to the case where too many free radicals are generated, which would drastically broaden the signals. The identification of potential intermediate molecular species and degradation products requires a more sophisticated tool than 1D NMR. This is why we turned to localized 2D homo- and heteronuclear experiments. Several authors have already developed localized heteronuclear correlation experiments, and even applied them in vivo on clinical imagers.[17,18,19,20] Here, given the cylindrical geometry of the NMR area and the rf shielding provided by the aluminium foils, it is sufficient to select a xy pixel instead of an xyz voxel. We have thus modified in accordance the original HSQC pulse sequence with sensitivity improvement[21] implemented on the spectrometer, principally in replacing the first two ^{1}H 90° hard pulses by frequency-selective ones simultaneous to magnetic field gradients (see Figure 3a). Note that the HSQC scheme was preferred to the HMQC one as the presence of multiquanta coherences which relaxation is accelerated is detrimental to the sensitivity of the experiment. Due to a possible spatial spreading of B_1 field linked to the presence of the electrode, we have preferred to render the 90° pulses spatially-selective instead of the 180° refocusing pulses. Thus the first ^{1}H 90° pulse excites the protons placed inside a slice along x. The INEPT scheme occurs there. In order to ensure that the final amount of magnetization flipped along z by the second 90° pulse only depends on the C-H coupling constant, and not on the spatial position of the spins along the gradient direction, a second gradient of the same sign and amplitude as the slice gradient but of half duration (the tilting of the magnetization in the transverse plane by the soft pulse is considered to occur in the middle of the pulse) is applied after the 180° ^{1}H pulse. Note that the carbon 90° pulse is shifted just after the gradient of the second slice selection so that it is not spatially selective.

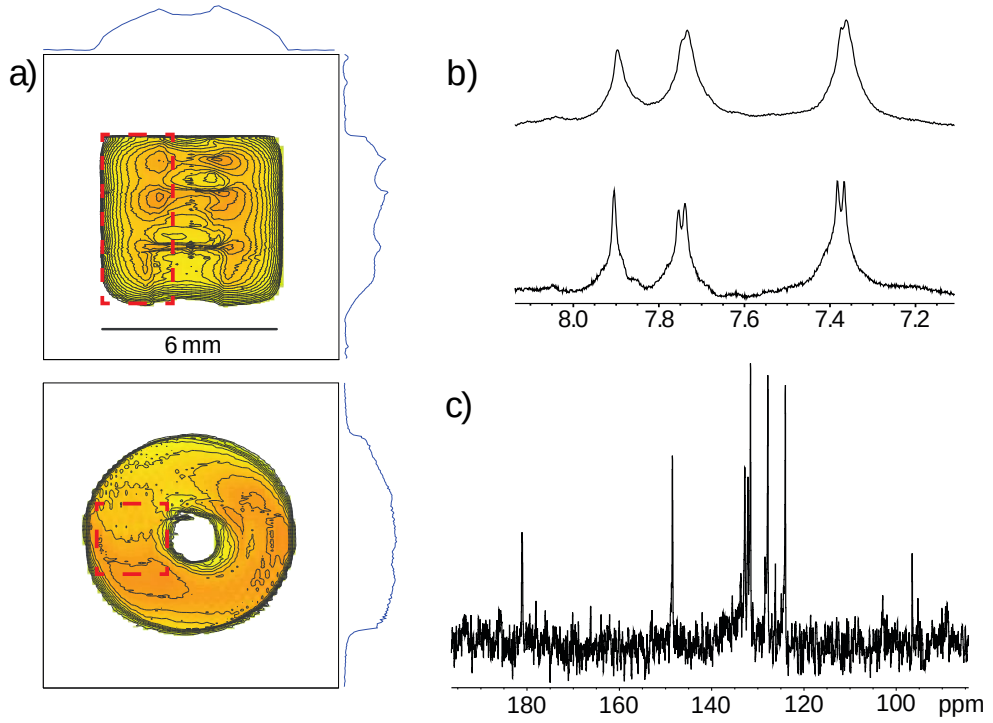


Figure 2. a) 2D 1H gradient echo images of the NMR reservoir. The presence of the electrode is clearly visible. b) Comparison between normal (4 scans, up) and localized (8 scans, down) 1H spectra of 2,7-AQDS (0.5 M). The selected area corresponds to the region delimited by the red dashed lines in a). c) 1H-decoupled 13C spectrum of 2,7-AQDS (0.5 M; 128 scans).

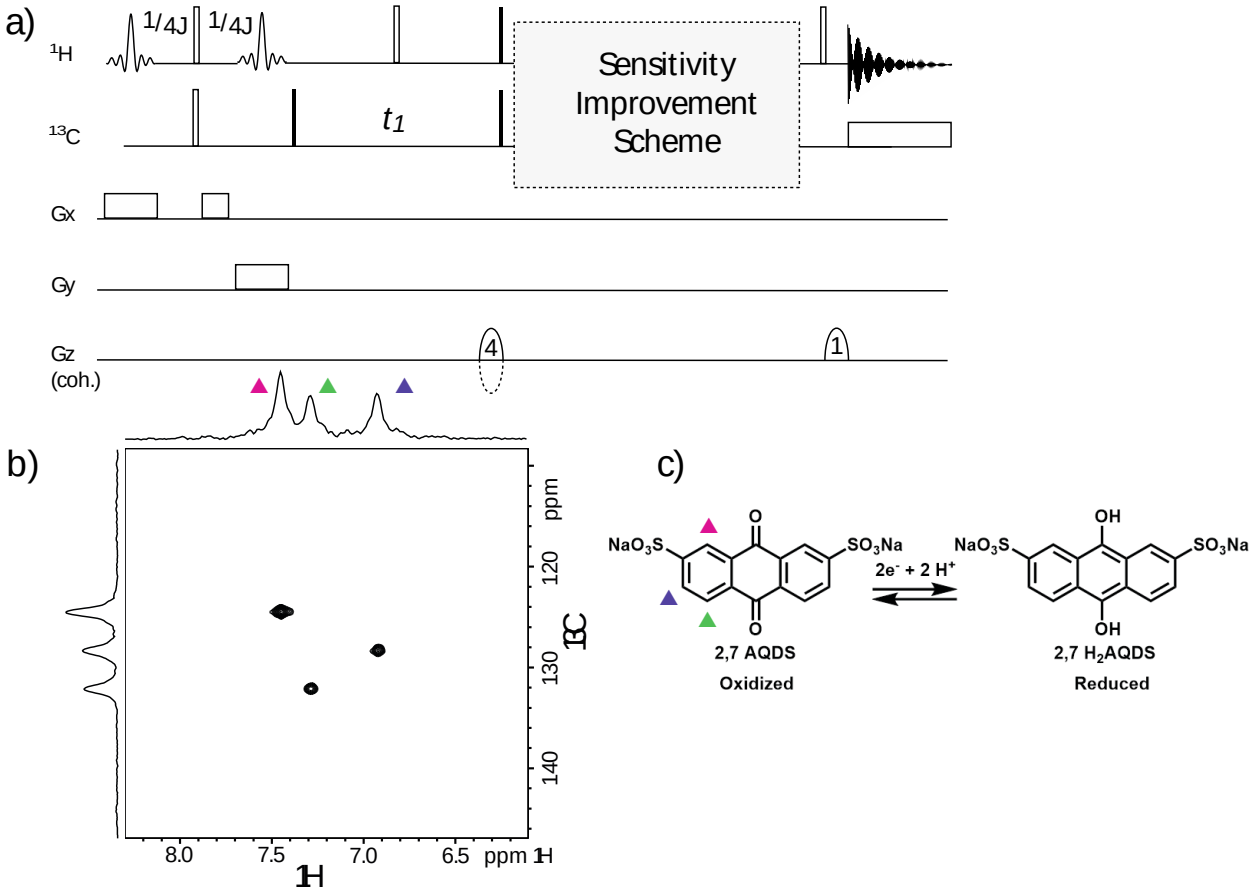


Figure 3. a) Pulse sequence of the localized 2D HSQC experiment. The black and white rectangles indicate 90° and 180° hard pulses respectively, the 90° soft pulses being represented by a sinc shape. For the z gradients, their relative value is indicated inside the shape. The dashed negative shape indicates the echo-antiecho scheme for quadrature in the indirect dimension. b) 1H-13C HSQC performed on the oxidized form of 2,7-AQDS at 0.5 M (experiment time: 1h) inside the 2.4 x 2.4 mm pixel of the NMR reservoir drawn in previous Figure. c) Structure of 2,7-AQDS, under its oxidized and reduced forms.

While x and y gradients serve for spatial localization, the z gradients are used for coherence selection. The factor 4 between the two gradients allows to select only ^{13}C coherences that have evolved during t1 and transferred to the protons for detection.

Figure 3b displays the contour plot of the localized HSQC recorded in one hour on a 0.5 M solution of 2,7-AQDS. The one-bond ^{1}H-^{13}C correlations are quite clean. This contour plot can be compared with the one recorded on the same sample without localization. On Fig. S7 of the Supp. Info., the improvement in spectral resolution is obvious in the 1H dimension.

In addition to the identification of the molecular structure of compounds in solution, this device allows the measurement of two other important parameters: i- measurement of the diffusion coefficient of the molecular species in solution, according to the pH, concentration and temperature conditions 2,7-AQDS can be subjected to multimerization[22] which can be detected through self-diffusion experiments. ii- solution flow monitoring, the operation of a redox flow battery requires electrolytes circulation, so as to renew the molecular species at the electrodes surface. In our battery, where this flow is driven by an inert gas, this monitoring is essential. The solution flux can be characterized by NMR velocimetry experiments, as shown in Figure 4.

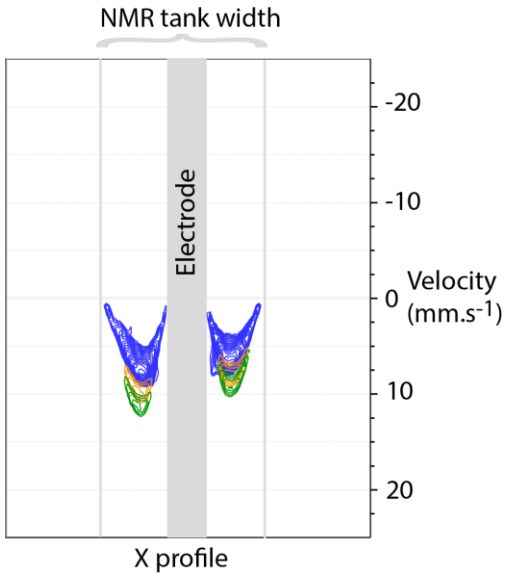


Figure 4. Velocity profiles of the solution inside the NMR tank, with a nitrogen flow of 1 mL/min (blue), 2 mL/min (orange) and 3 mL/min (green).

This point is important, since an insufficient level of liquid in the upper part of the insert prevents the proper functioning of the bubble pump and thus the circulation of the electrolyte solution. In this case, the solution 'oscillates' without a net solution displacement (see Fig. S8 of the Supp. Info.). Thus, this simple and fast experiment (less than 1 min) is sufficient to periodically ensure that the solution is flowing.

As an application, we have monitored the evolution of 2,7-AQDS during cycles of charge (reduction) and discharge (oxidation). The first step has been to perform a cyclic voltammetry to define the oxidation and reduction voltage peaks. Figure S9 of the Supp. Info. shows that these peaks appear at +0.3 V and -0.6 V. Obviously a magnetic field has an effect on mass transport of charged species, proportional to the cross product between magnetic field intensity and current density.[15] This can lead to complex flow pattern, but, as already stated, due to the design of the cell this so-called magneto-hydrodynamic effect is reduced. This can be checked on Figure S10 of the Supporting Information, which compares the cyclic voltammograms recorded with and without magnetic field.

Figure 5 displays the 1H spectra of 2,7-AQDS 50 mM in H2SO4 0.5 M at three different steps after a voltage of -0.5 V has been applied (see the corresponding chronoamperometry in Fig. S11). The medium in which the counter-electrode immersed is also H2SO4 0.5 M. A -0.5 V voltage is chosen instead of -0.6 V, in order to avoid the formation of hydrogen bubbles at the surface of the WE electrode that reduces the spectral homogeneity.

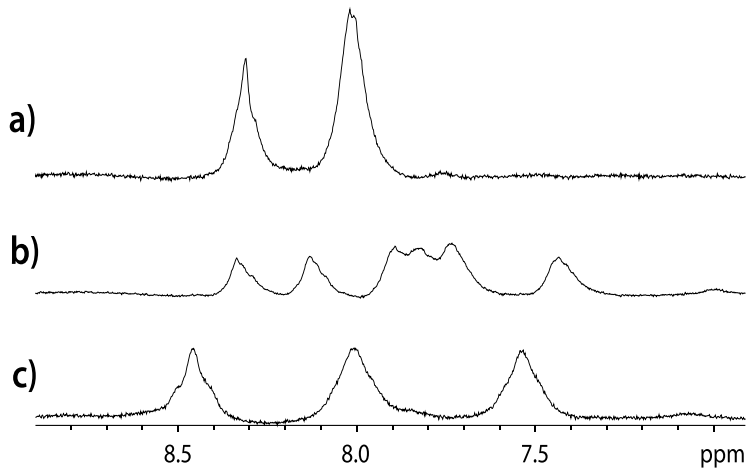


Figure 5. Three 1H spectra of 2,7-AQDS during a reduction process. a) Oxidized form; b) Intermediate form; c) Reduced form.

A more complete representation is a contour plot of the successive spectra recorded each 5 minutes during the reduction steps (Figure 6a). More meaningful, Figure 6b displays the spectra as a function of the number of Coulombs that are exchanged. Figure 6c shows the 3D profile of the time evolution of the spectra, and Figure 6d the sum of the peak area as a function of the number of Coulombs exchanged. Figs 6e-h follow the same principle for an oxidation step, in which a voltage of +0.45 V is applied. The corresponding chronoamperometry is displayed in Figure S12.

From Figure 6b it is immediate to see that the first and last spectra correspond to the oxidized and reduced forms of 2,7-AQDS, respectively. Given the equation Q = c.V.n.F, where Q stands for the num-

ber of Coulombs for a complete electrochemical reaction, c the 2,7-AQDS concentration (50 mM), V the solution volume (here 1.8 mL), n the number of exchanged electrons (2 for 2,7-AQDS) and F the Faraday constant, 17 Coulombs are expected for a full redox conversion. This is approximatively what is observed in Figs 6b and 6d (for the return to the oxidized state, the NMR acquisition started well after the electrochemical reaction).

From these graphs, several observations can be made. i) At the beginning of both the reduction step and the oxidation step, the three aromatic proton signals experience a high field shift, with an almost identical slope variation. ii) A progressive loss of global intensity occurs, before the appearance of the other form. iii) The protons of the new form are then subjected to a downfield shift and the global intensity re-increases.

The change in the global line intensities (Fig. 6d and h) indicates that some intermediates of the reaction are radical species, as already observed by Wiberg et al.[22] Note that their predominance occurs at ca. 11 Coulombs, i. e. 60% of the oxidation.

Also the initial high field chemical shift variation for the three aromatic protons and in the second part the subsequent low field variation suggest that heterodimers associating 2,7-AQDS and $H_2$2,7-AQDS are more stable than 2,7-AQDS-2,7-AQDS and H_2(2,7-AQDS)-H_2(2,7-AQDS) homodimers, probably favoured by hydrogen bonds. This can be explained by the following reasoning, leaving aside the monomer/homodimer equilibrium.

For both the oxidized and the reduced species, each proton chemical shift experiencing fast exchange between the monomeric form and the heterodimeric form can be expressed as:

$$\delta = x\,\delta_M + (1-x)\,\delta_D$$

where δ_M and δ_D stand for the chemical shift of the monomer and of the dimer, respectively,

and x = [Monomer]/([Monomer]+[Dimer]) is the molar fraction of monomer. For the following, we will refer to the oxidized, reduced, and heterodimeric forms as O, R and O-R, respectively.

In accordance with Carney et al.[23,] it is known that the passage from the oxidized monomeric form to the (homo)dimeric form due to concentration increase leads to an upfield shift of the three proton signals (from 8.4, 8.15, 8.0 to 7.7, 7.05, 7.55 ppm in H_2SO_4 0.5 M). Here there is no reason to imagine that the concentration increases during the redox cycle, but rather that the high field shift is due to heterodimers between the oxidized and reduced forms.

At about half the charge (or discharge) the second monomeric form becomes predominant, and as the homodimers are less probable the chemical shifts start to re-increase. At this step, 6 distinct ^{1}H peaks are clearly visible (Fig. 5b), corresponding to the six protons of the heterodimer. To confirm our hypothesis, the same 2D self-diffusion NMR experiment (DOSY) has been performed on the oxidized state and at this step where 6 peaks appear (Fig. S13), both experiments being performed in the absence of solution flow and electric current. While it has been checked that the water diffusion coefficient remains constant at 2.2 10^{-9} m^2s^{-1}, the diffusion coefficient of the aromatic protons decreases from 0.48 10^{-9} m^2s^{-1} to 0.40 10^{-9} m^2s^{-1}. Passing from a fast mixture of monomer/homodimer to the heterodimer is not expected to divide by 2 the diffusion coefficient, as the π-stacking arrangement is not prone to significantly modify the hydrodynamic radius of the molecule.[24] Thus although the self-diffusion experiment is only qualitative, it comforts our assertions. To confirm or deny our hypotheses we have undertaken theoretical chemistry calculations.

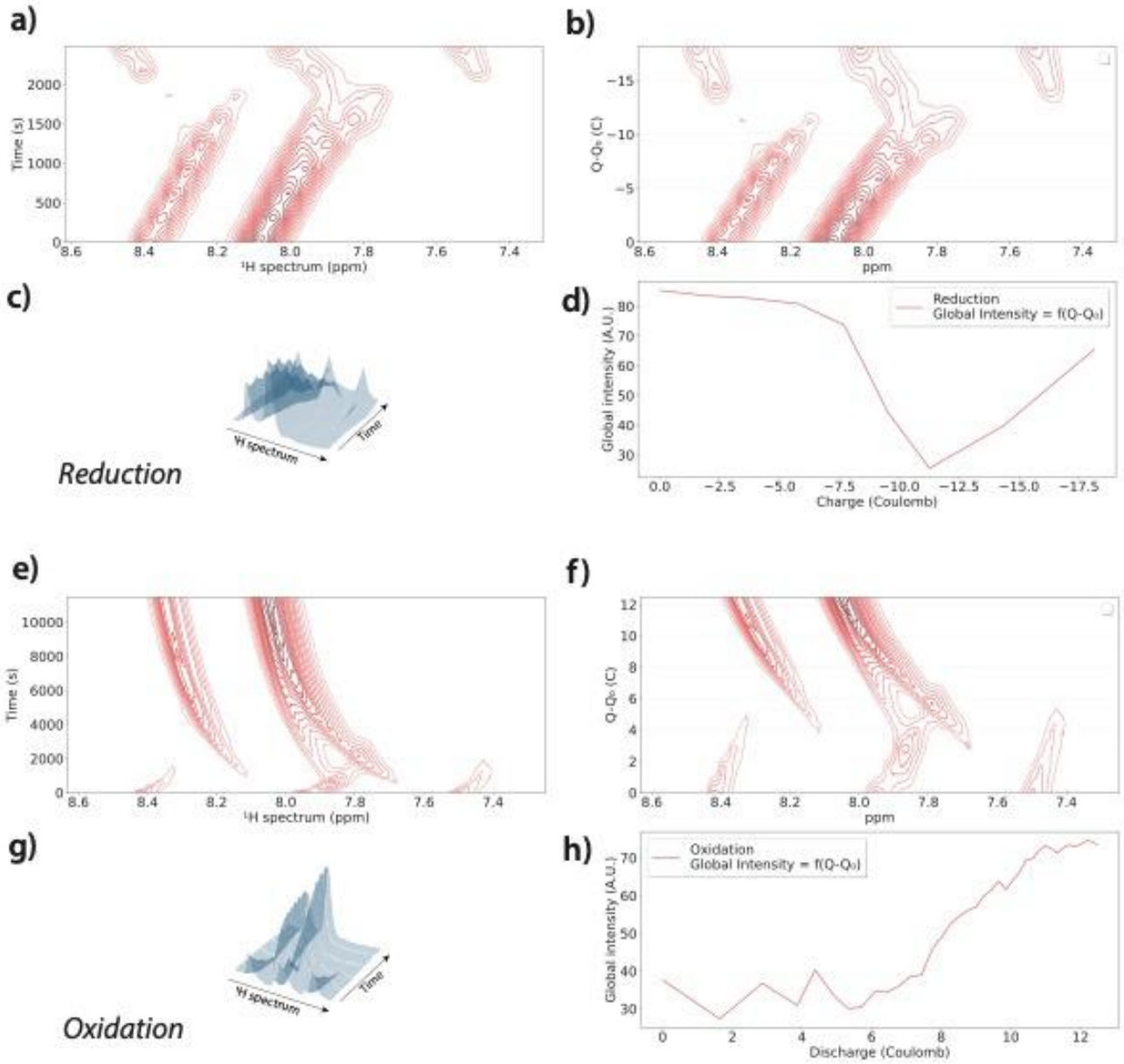


Figure 6. a-d) Evolution of the 1H NMR spectrum of 2,7-AQDS (50 mM in H2SO4 0.5 M) during the reduction step (charge of the mini-battery). a) Contour plot of the spectra according to time; b) Spectra according to the number of Coulombs exchanged; c) 3D view of these spectra; d) Sum of the peak intensities as a function of the number of Coulombs exchanged. e-f) Evolution of the 1H NMR spectrum of 2,7-AQDS during the oxidation step (discharge of the mini-battery). e) Contour plot of the spectra according to time; f) Spectra according to the number of Coulombs exchanged; g) 3D view of these spectra; h) Sum of the peak intensities as a function of the number of Coulombs exchanged.

For the dimers, various π–π stacking and hydrogen bonding motifs are possible. We implemented quantum chemical, multilevel modelling workflows for the determination of the 2,7-AQDS dimerization preferences. This is accomplished by a conformer search based on the CREST sampling software.[25] The main goal of the conformer search is to find the energetically most favourable conformers. For the final geometry optimization (and the final free energy calculation) of the most stable conformers, we used the composite DFT method r2SCAN-3c[26] with the ORCA 5.0.3 program.[27]

The binding free energies (ΔG) for the formation of an A-B dimer (used for the cases of the O-O, R-R and O-R dimers) are defined as $\Delta G_{bind} = G_{AB} - G_A - G_B$. The most stable dimer geometries and binding free energies are shown in Figure 7.

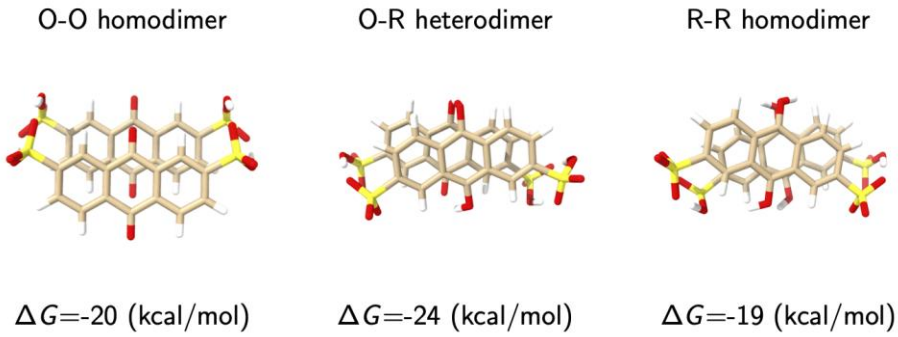


Figure 7. Most stable geometries and binding free energies of the dimers appearing during the redox cycle.

These quantum chemistry results indicate that the oxidized 2,7-AQDS and the reduced 2,7-AQDS ligands can form together a stable heterodimer in preference to homodimers. This is in good accordance with literature studies who demonstrate that at the low concentration used for our 2,7-AQDS electrolyte, the 2,7-AQDS dimer is not the main species.[22] The stabilization of the heterodimer is mainly due to H-bonds and van der Waals attractive interaction as graphically revealed in Figure 8 from the Interaction Region Indicator (IRI)28 calculated with the Multiwfn program.[29] Note that Tong et al.,[30] using UV-Vis spectroscopy, also evidenced an heterodimer stabilized via hydrogen bonding between oxidized and reduced quinone forms in solution. Thus, in the scenario that we envision (depicted in Figure 9), in our experimental conditions four main species are in fast equilibrium at the NMR time scale during cycling: the 2,7-AQDS and H_2(2,7-AQDS) monomers, the 2,7-AQDS/ H_2(2,7-AQDS) heterodimer and the H(2,7-AQDS)• radicals. The relative concentration of each species evolves with the state of charge. As expected, the concentrations of the heterodimer and of the H(2,7-AQDS)• radicals are maximum when half the theoretical number of electrons is transferred both in charge and in discharge. This mechanism is in accordance with previous works performed by Wiberg et al.[22]

Our experimental setup obviously does not allow yet direct detection of the free radical states, which would require an in situ system including both NMR and EPR.[7,8] But this low-cost, custom-made, disposable device has some interesting potentialities. First of all, the low volumes of solution required will enable the study of expensive organic electrolytes, and will induce short cycling times. Second, the observation of other nuclei such as lithium or sodium will only require a change of the tuning capacitor at the base of the insert, which can be done at low cost. It gives this device a high versatility. Third, the device as designed is based on a micro-imaging probe, which allows us to use localized spectroscopy, and to obtain reasonable spectral homogeneity, even in the most electrochemically interesting region, which is that surrounding the working electrode. Last, the availability of pulsed field gradients also opens the way to characterization techniques of the flow or of the molecular species, such as velocimetry, self-diffusion experiments.

The perspectives are now to replace our polymer inserts, which however resist well to acidic environments, by inserts still 3D printed, but in more inert ceramic or glass, using the low-cost processes proposed among others by Kotz et al.[31] based on the initial use of organic inks loaded in SiO_2, Al_2O_3 or ZrO_2 particles.

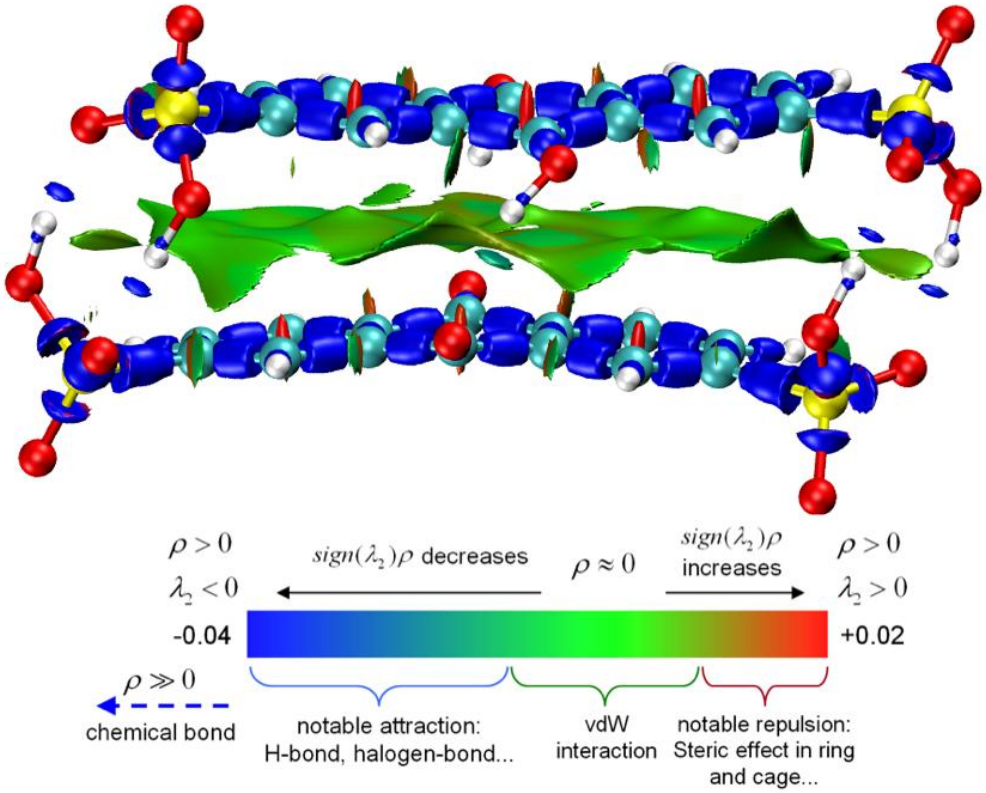


Figure 8. Weak interaction and chemical bond regions from IRI map for the 2,7-AQDS / 2,7-H2AQDS heterodimer.

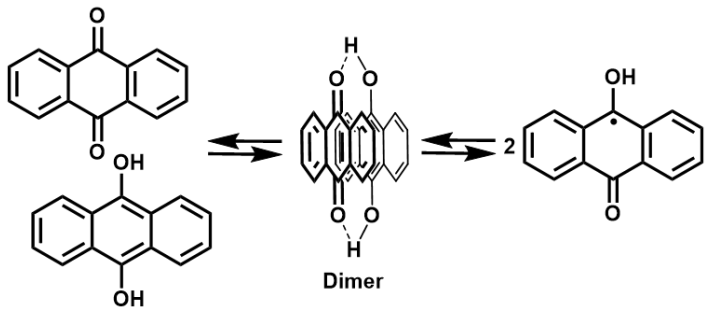


Figure 9. a) Scheme of the hypothetical processes occurring during the charge/discharge cycles for 2,7-AQDS. The sulfonate groups are not displayed for sake of clarity.

EXPERIMENTAL SECTION

Building of the ORFB

The CAD of the battery body was made with SolidWorks (Dassault System) and the piece bodies were built by additive manufacturing using a PolyJet Objet30 printer (Stratasys) equipped with PMMA-based VeroClear resin. The saddle coils were made with 0.7 mm diameter copper wire with two loops for the outer 13C coil and one loop for the 1H inner coil. The tuning capacitors were MLCC KEMET ceramics. The rf shielding of the back channel was made with a 0.02 mm width aluminium foil. The working and reference electrodes were welded on 0.8 mm copper wire insulated by heat-shrink tube itself welded on a print card board (designed on KiCad electronics CAD software) for interface with the potentiostat connectors. The shape of the PCB was mechanically adapted to interface with a silicon joint cut to size for the gas proof of the receptacle limiting any oxidation reaction with air.

Electrochemistry

Electrochemical measurements were performed with a SP 150 potentiometer (Biologic). The working electrode (WE) was a 1 mm-diameter glassy carbon rod type 2 (Alfa Aesar) polished with a water-alumina slurry 0.05 µm (Sigma-Aldrich) before each experiment. The reference electrode (RE) was a 0.2 mm-diameter silver wire poured in Ag/AgCl Ink (ALS) and dried with hot air (121°C during 15 min); a homogeneous coating with a cation-exchange Nafion D2020 solution (Ion Power) was applied to provide protection and guarantee a stable potential in acidic conditions. The counter electrode was a 1.55 mm-diameter 99.9% platinum wire cleaned with 10% nitric acid before each experiment.

NMR

NMR experiments were performed at room temperature on a narrow-bore 11.7 T Bruker Avance II spectrometer equipped with 3-axes field gradients of max. amplitude 200 $G.cm^{-1}$. The NMR probe body on which the 3D-printed insert was plugged was a dual-channel Bruker Micro-5. Self-diffusion experiments used stimulated echo and longitudinal eddy current delay (LED32), with a gradient duration δ of 1 ms and inter-gradient delay Δ of 150 ms. The gradients had a sine shape and the indirect dimension of the experiments contained 16 points linearly spaced from 4 to 90 G/cm.

Processing of the operando NMR data

The evolution of the anthraquinone derivatives during reduction or oxidation was monitored by one-dimensional 1H spectra performed with or without spatial localization, and then assembled in a 2D map, with the time as ordinate (Figs 6a and 6e). A Python program then established a temporal correlation between chronoamperometry and NMR, in order to transform the time ordinate axis into a number of exchanged Coulombs, more useful for analysis (Figs 6b and 6f). In the same program, the 3D view of the spectra is computed (Figs 6c and 6g), as well as the curve giving the sum of the aromatic peak intensities as a number of Coulombs (Figs 6d and 6h). This program is available upon request to the authors.

ASSOCIATED CONTENT

Supporting Information

Full-size reproduction of Fig. 1c; 1H image of the cell without the aluminum shields; CAD drawings of the mini-battery; 2D maps of the localized and non-localized 1H-13C HSQC experiments performed on 2,7-AQDS; 1H NMR velocimetry experiment in the presence of an insufficient solution level; Cyclic Voltammetry; Chronoamperometry curves; DOSY experiments at the oxidized and intermediate states (PDF).

AUTHOR INFORMATION

Corresponding Author

* patrick.berthault@cea.fr

Author Contributions

The manuscript was written through contributions of all authors. All authors have given approval to the final version of the manuscript.

ACKNOWLEDGMENT

Supports from the French Ministry of Research (project 17-LCV2-0002-01 LabCom DESIR) and from CEA (Programmes Transverses de Compétences; project ROBO3D) are acknowledged.

REFERENCES

(1) Kwabi, D. G.; Ji, Y.; Aziz, M. J. Electrolyte Lifetime in Aqueous Organic Redox Flow Batteries: A Critical Review. Chem. Rev. 2020, 120 (14), 6467–6489. https://doi.org/10.1021/acs.chemrev.9b00599.

(2) Goulet, M.-A.; Tong, L.; Pollack, D. A.; Tabor, D. P.; Odom, S. A.; Aspuru-Guzik, A.; Kwan, E. E.; Gordon, R. G.; Aziz, M. J. Extending the Lifetime of Organic Flow Batteries via Redox State Management. J. Am. Chem. Soc. 2020, 141 (20), 8014–8019. https://doi.org/10.1021/jacs.8b13295.

(3) Kuwana, Theodore.; Darlington, R. K.; Leedy, D. W. Electrochemical Studies Using Conducting Glass Indicator Electrodes. Anal. Chem. 1964, 36 (10), 2023–2025. https://doi.org/10.1021/ac60216a003.

(4) Jones, A. E.; Ejigu, A.; Wang, B.; Adams, R. W.; Bissett, M. A.; Dryfe, R. A. W. Quinone Voltammetry for Redox-Flow Battery Applications. J. Electroanal. Chem. 2022, 920, 116572. https://doi.org/10.1016/j.jelechem.2022.116572.

(5) Richards, J. A.; Evans, D. H. Flow Cell for Electrolysis within the Probe of a Nuclear Magnetic Resonance Spectrometer. Anal. Chem. 1975, 47 (6), 964–966. https://doi.org/10.1021/ac60356a016.

(6) Albert, K.; Dreher, E.-L.; Straub, H.; Rieker, A. Monitoring Electrochemical Reactions by 13C NMR Spectroscopy. Magn. Reson. Chem. 1987, 25 (10), 919–922. https://doi.org/10.1002/mrc.1260251017.

(7) Jing, Y.; Zhao, E. W.; Goulet, M.-A.; Bahari, M.; Fell, E. M.; Jin, S.; Davoodi, A.; Jónsson, E.; Wu, M.; Grey, C. P.; Gordon, R. G.; Aziz, M. J. In Situ Electrochemical Recomposition of Decomposed Redox-Active Species in Aqueous Organic Flow Batteries. Nat. Chem. 2022, 14 (10), 1103–1109. https://doi.org/10.1038/s41557-022-00967-4.

(8) Zhao, E. W.; Jónsson, E.; Jethwa, R. B.; Hey, D.; Lyu, D.; Brookfield, A.; Klusener, P. A. A.; Collison, D.; Grey, C. P. Coupled In Situ NMR and EPR Studies Reveal the Electron Transfer Rate and Electrolyte Decomposition in Redox Flow Batteries. J. Am. Chem. Soc. 2021, 143 (4), 1885–1895. https://doi.org/10.1021/jacs.0c10650.

(9) McKenzie, E. C. R.; Hosseini, S.; Petro, A. G. C.; Rudman, K. K.; Gerroll, B. H. R.; Mubarak, M. S.; Baker, L. A.; Little, R. D. Versatile Tools for Understanding Electrosynthetic Mechanisms. Chem. Rev. 2022, 122 (3), 3292–3335. https://doi.org/10.1021/acs.chemrev.1c00471.

(10) Causier, A.; Carret, G.; Boutin, C.; Berthelot, T.; Berthault, P. 3D-Printed System Optimizing Dissolution of Hyperpolarized Gaseous Species for Micro-Sized NMR. Lab. Chip 2015, 15 (9), 2049–2054. https://doi.org/10.1039/C5LC00193E.

(11) Carret, G.; Berthelot, T.; Berthault, P. Enhancing NMR of Nonrelaxing Species Using a Controlled Flow Motion and a Miniaturized Circuit. Anal. Chem. 2017, 89 (5), 2995–3000. https://doi.org/10.1021/acs.analchem.6b04488.

(12) Carret, G.; Berthelot, T.; Berthault, P. Inductive Coupling and Flow for Increased NMR Sensitivity. Anal. Chem. 2018, 90 (19), 11169–11173. https://doi.org/10.1021/acs.analchem.8b01775.

(13) Huskinson, B.; Marshak, M. P.; Suh, C.; Er, S.; Gerhardt, M. R.; Galvin, C. J.; Chen, X.; Aspuru-Guzik, A.; Gordon, R. G.; Aziz, M. J. A Metal-Free Organic–Inorganic Aqueous Flow Battery. Nature 2014, 505 (7482), 195–198. https://doi.org/10.1038/nature12909.

(14) Gerhardt, M. R.; Tong, L.; Gómez-Bombarelli, R.; Chen, Q.; Marshak, M. P.; Galvin, C. J.; Aspuru-Guzik, A.; Gordon, R. G.; Aziz, M. J. Anthraquinone Derivatives in Aqueous Flow Batteries. Adv. Energy Mater. 2017, 7 (8), 1601488. https://doi.org/10.1002/aenm.201601488.

(15) Ferreira Gomes, B.; Ferreira da Silva, P.; Silva Lobo, C. M.; da Silva Santos, M.; Colnago, L. A. Strong Magnetoelectrolysis Effect during Electrochemical Reaction Monitored in Situ by High-Resolution NMR Spectroscopy. Anal. Chim. Acta 2017, 983, 91–95. https://doi.org/10.1016/j.aca.2017.06.008.

(16) Benders, S.; Gomes, B. F.; Carmo, M.; Colnago, L. A.; Blümich, B. In-Situ MRI Velocimetry of the Magnetohydrodynamic Effect in Electrochemical Cells. J. Magn. Reson. 2020, 312, 106692. https://doi.org/10.1016/j.jmr.2020.106692.

(17) Watanabe, H.; Ishihara, Y.; Okamoto, K.; Oshio, K.; Kanamatsu, T.; Tsukada, Y. 3D Localized 1H-13C Heteronuclear Single-Quantum Coherence Correlation Spectroscopy in Vivo. Magn. Reson. Med. 2000, 43 (2), 200–210. https://doi.org/10.1002/(SICI)1522-2594(200002)43:2<200::AID-MRM6>3.0.CO;2-H.

(18) De Feyter, H. M.; Herzog, R. I.; Steensma, B. R.; Klomp, D. W. J.; Brown, P. B.; Mason, G. F.; Rothman, D. L.; de Graaf, R. A. Selective Proton-Observed, Carbon-Edited (SelPOCE) MRS Method for Measurement of Glutamate and Glutamine 13 C-Labeling in the Human Frontal Cortex. Magn. Reson. Med. 2018, 80 (1), 11–20. https://doi.org/10.1002/mrm.27003.

(19) Kanamori, K.; Ross, B. D. In Vivo Detection of 15N-Coupled Protons in Rat Brain by ISIS Localization and Multiple-Quantum Editing. J. Magn. Reson. 1999, 139 (2), 240–249. https://doi.org/10.1006/jmre.1999.1764.

(20) Méric, P.; Autret, G.; Doan, B. T.; Gillet, B.; Sébrié, C.; Beloeil, J.-C. In Vivo 2D Magnetic Resonance Spectroscopy of Small Animals. Magn. Reson. Mater. Phys. Biol. Med. 2004, 17 (3), 317–338. https://doi.org/10.1007/s10334-004-0084-2.

(21) Schleucher, J.; Schwendinger, M.; Sattler, M.; Schmidt, P.; Schedletzky, O.; Glaser, S. J.; Sørensen, O. W.; Griesinger, C. A General Enhancement Scheme in Heteronuclear Multidimensional NMR Employing Pulsed Field Gradients. J. Biomol. NMR 1994, 4 (2), 301–306. https://doi.org/10.1007/BF00175254.

(22) Wiberg, C.; Carney, T. J.; Brushett, F.; Ahlberg, E.; Wang, E. Dimerization of 9,10-Anthraquinone-2,7-Disulfonic Acid (AQDS). Electrochimica Acta 2019, 317, 478–485. https://doi.org/10.1016/j.electacta.2019.05.134.

(23) Carney, T. J.; Collins, S. J.; Moore, J. S.; Brushett, F. R. Concentration-Dependent Dimerization of Anthraquinone Disulfonic Acid and Its Impact on Charge Storage. Chem. Mater. 2017, 29 (11), 4801–4810. https://doi.org/10.1021/acs.chemmater.7b00616.

(24) Hamelin, B.; Jullien, L.; Derouet, C.; Hervé du Penhoat, C.; Berthault, P. Self-Assembly of a Molecular Capsule Driven by Electrostatic Interaction in Aqueous Solution. J. Am. Chem. Soc. 1998, 120 (33), 8438–8447. https://doi.org/10.1021/ja980046g.

(25) Pracht, P.; Bohle, F.; Grimme, S. Automated Exploration of the Low-Energy Chemical Space with Fast Quantum Chemical Methods. Phys. Chem. Chem. Phys. 2020, 22 (14), 7169–7192. https://doi.org/10.1039/C9CP06869D.

(26) Grimme, S.; Hansen, A.; Ehlert, S.; Mewes, J.-M. R 2 SCAN-3c: A “Swiss Army Knife” Composite Electronic-Structure Method. J. Chem. Phys. 2021, 154 (6), 064103. https://doi.org/10.1063/5.0040021.

(27) Neese, F. Software Update: The ORCA Program System—Version 5.0. WIREs Comput. Mol. Sci. 2022, 12 (5). https://doi.org/10.1002/wcms.1606.

(28) Lu, T.; Chen, Q. Interaction Region Indicator: A Simple Real Space Function Clearly Revealing Both Chemical Bonds and Weak Interactions. Chemistry–Methods 2021, 1 (5), 231–239. https://doi.org/10.1002/cmtd.202100007.

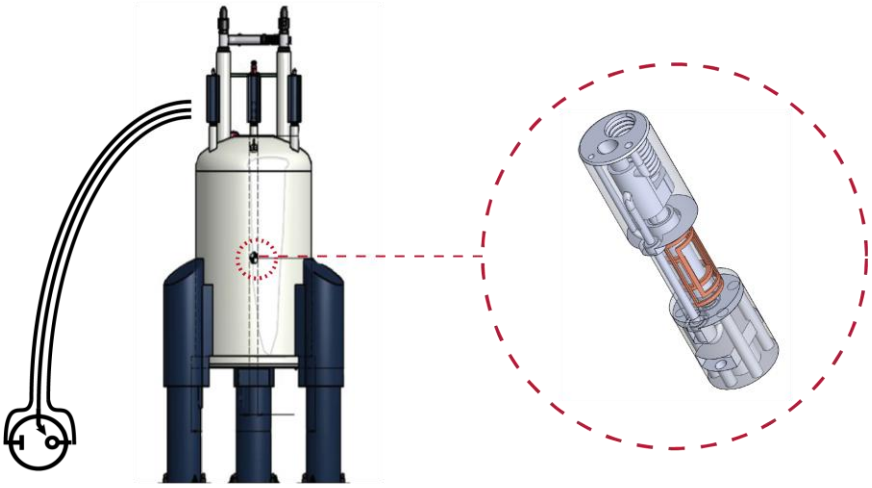
(29) Lu, T.; Chen, F. Multiwfn: A Multifunctional Wavefunction Analyzer. J. Comput. Chem. 2012, 33 (5), 580–592. https://doi.org/10.1002/jcc.22885.

(30) Tong, L.; Chen, Q.; Wong, A. A.; Gómez-Bombarelli, R.; Aspuru-Guzik, A.; Gordon, R. G.; Aziz, M. J. UV-Vis Spectrophotometry of Quinone Flow Battery Electrolyte for in Situ Monitoring and Improved Electrochemical Modeling of Potential and Quinhydrone Formation. Phys. Chem. Chem. Phys. 2017, 19 (47), 31684–31691. https://doi.org/10.1039/C7CP05881K.

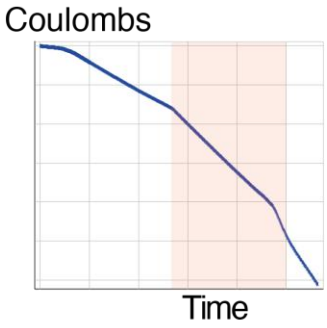
(31) Kotz, F.; Arnold, K.; Bauer, W.; Schild, D.; Keller, N.; Sachsenheimer, K.; Nargang, T. M.; Richter, C.; Helmer, D.; Rapp, B. E. Three-Dimensional Printing of Transparent Fused Silica Glass. Nature 2017, 544 (7650), 337–339. https://doi.org/10.1038/nature22061.

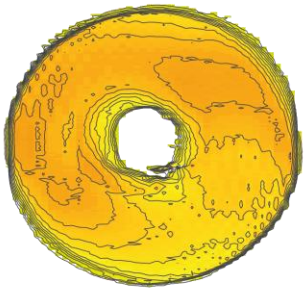
(32) Altieri, A. S.; Hinton, D. P.; Byrd, R. A. Association of Biomolecular Systems via Pulsed Field Gradient NMR Self-Diffusion Measurements. J. Am. Chem. Soc. 1995, 117 (28), 7566–7567. https://doi.org/10.1021/ja00133a039.

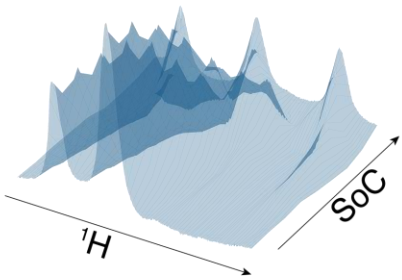
TABLE OF CONTENT



Electrochemistry **MRI** **Operando NMR**







Supporting Information

Table of Contents

Figure S1: 3D rendering of the mini-battery. Full-size reproduction of Fig. 1c 20

Figure S2: ^{1}H image of the cell without the aluminum shields 21

Figure S3: Drawing of the lower part of the mini redox-flow battery 22

Figure S4. Drawing of the middle part of the mini redox-flow battery 23

Figure S5: Drawing of the top part of the mini redox-flow battery 24

Figure S6: Drawing of the counter-electrode reservoir 25

Figure S7: Comparison between classical ^{1}H-^{13}C HSQC and spatially-localized ^{1}H-^{13}C HSQC performed on 2,7-AQDS 26

Figure S8: NMR velocimetry experiment performed with insufficient solution level in the cell 27

Figure S9: Cyclic Voltammetry recorded on the cell filled with oxidized 2,7-AQDS 50 mM in H_2SO_4 0.5 M 28

Figure S10: Influence of the magneto-hydrodynamic effect on the cyclic voltammetry 29

Figure S11: Chronoamperometry performed on the cell filled with oxidized 2,7-AQDS 50 mM in H_2SO_4 0.5 M 30

Figure S12: Chronoamperometry performed on the cell filled with reduced 2,7-H_2AQDS 50 mM in H_2SO_4 0.5 M 30

Figure S13: DOSY experiments performed on a) the oxidized state of AQDS, b) the intermediate state where 6 ^{1}H signals appear 31

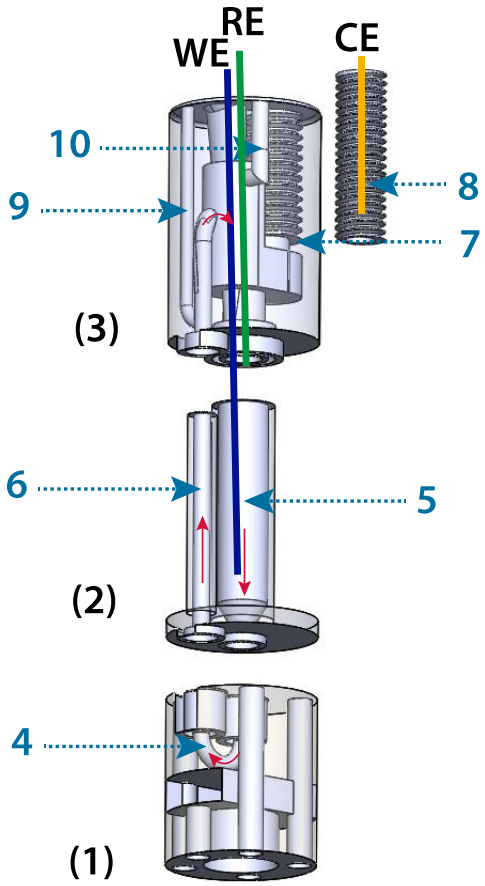


Figure S1. Full-size reproduction of Fig. 1c. 3D rendering of the bottom (1), middle (2) and top (3) parts of the device. (4) Solution circuit loop, (5) NMR area, (6) back channel, rf-isolated with aluminum foil, (7) proton-exchange membrane, (8) counter-electrode compartment, (9) nitrogen inlet, (10) nitrogen exhaust, WE: working electrode (glassy carbon), RE: reference electrode (Ag/AgCl), CE: counter-electrode (Pt). For the sake of clarity, neither the rf coils nor the copper connectors at the bottom of the part (1) for the electric connection to the NMR probehead are drawn.

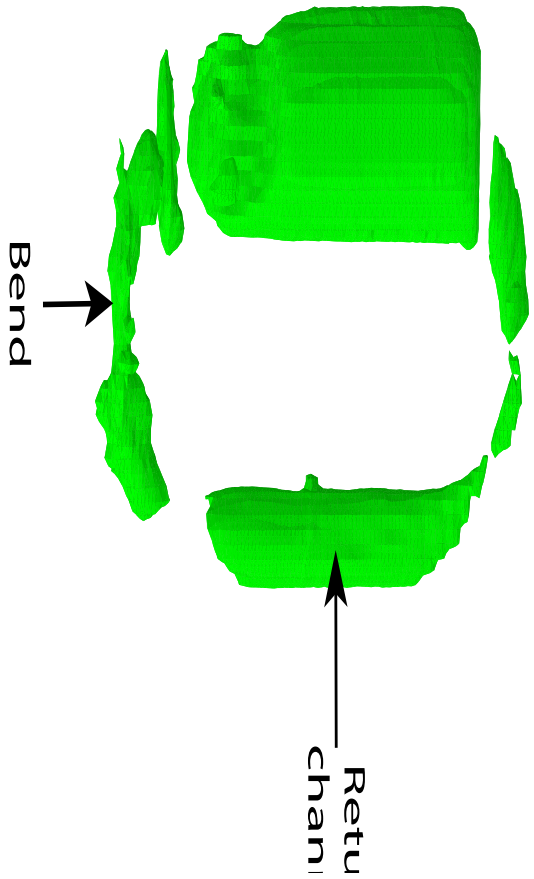


Figure S2. ^{1}H image of the cell without the aluminum shields. The water in the return channel and in the bend of the lower part is clearly visible. This leads to magnetic field heterogeneity (numerous air-liquid interfaces), which prevents a good spectral resolution.

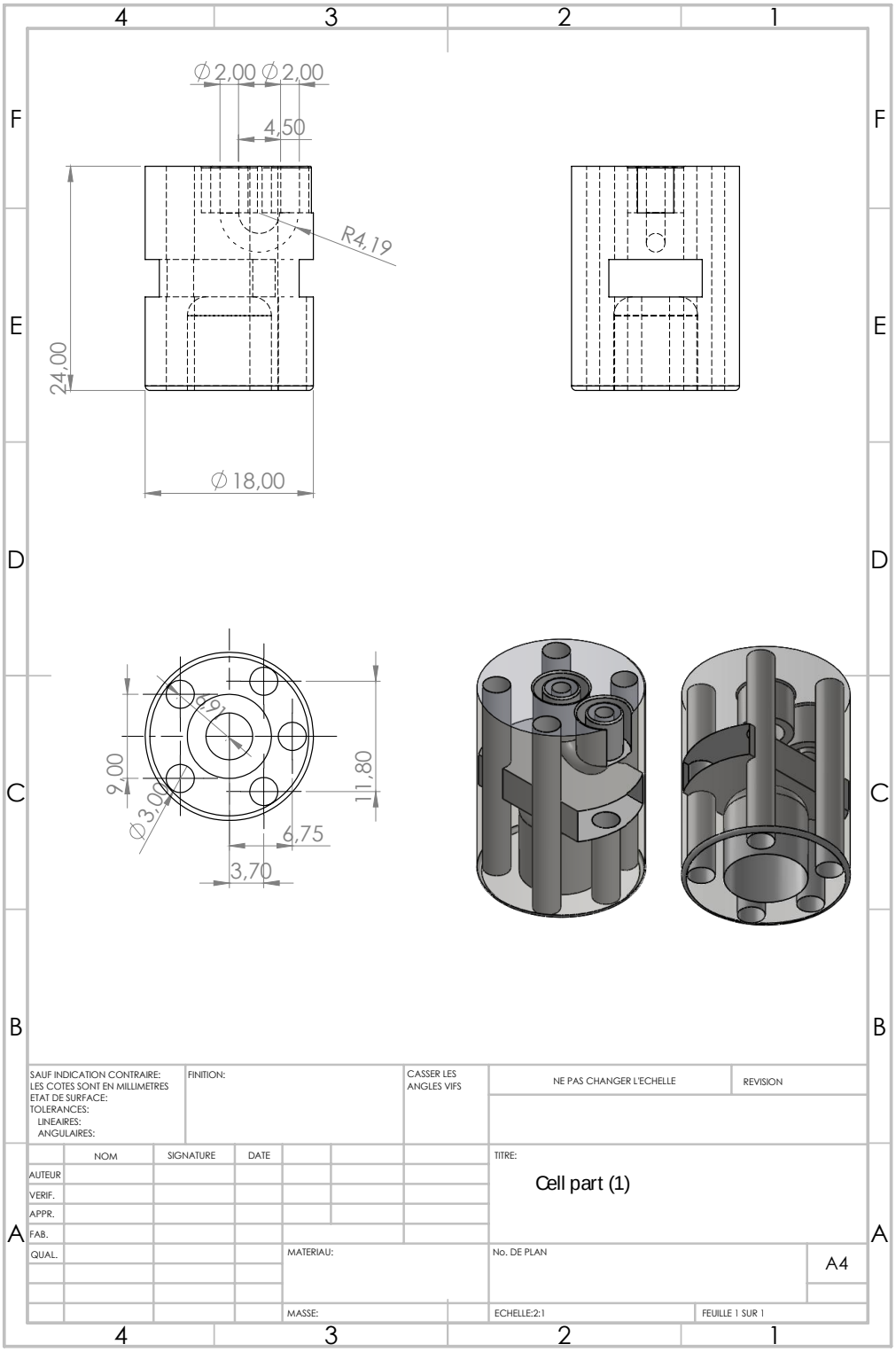


Figure S3. Drawing of the lower part of the mini redox-flow battery, to be plugged on a Bruker Micro-5 probe basis. The dimensions are in millimeters.

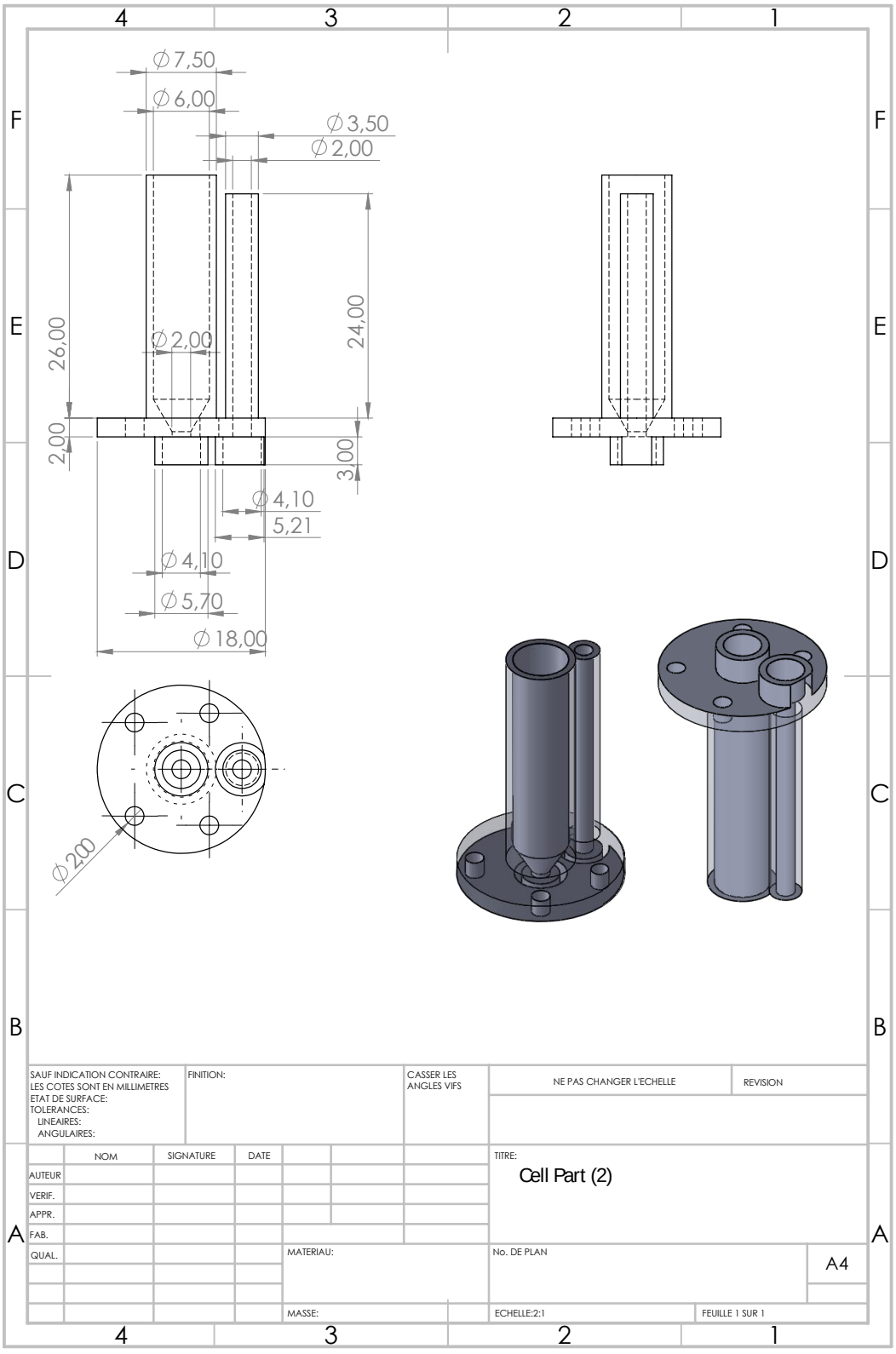


Figure S4. Drawing of the middle part of the mini redox-flow battery. The dimensions are in millimeters.

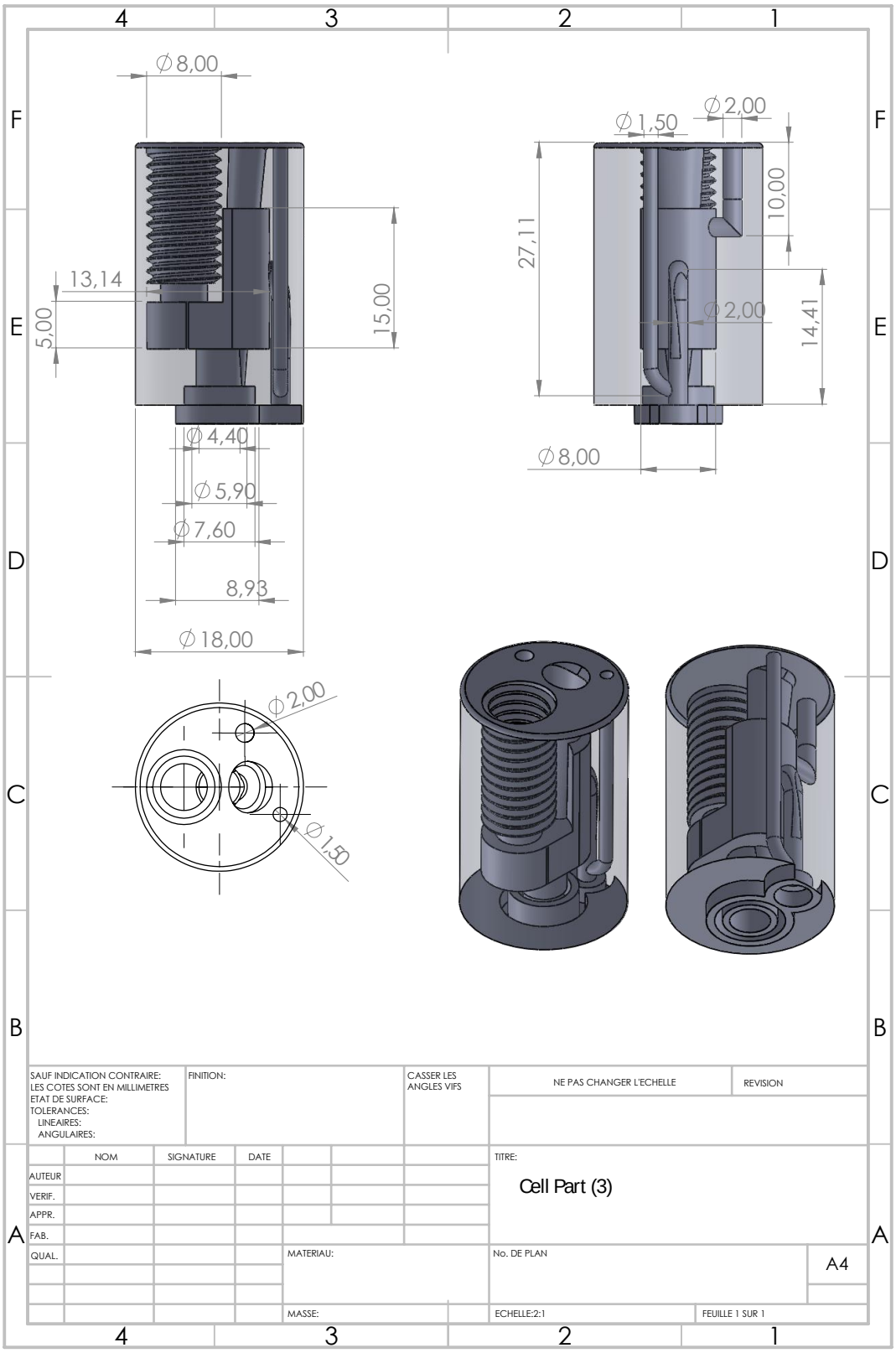


Figure S5. Drawing of the top part of the mini redox-flow battery. The dimensions are in millimeters.

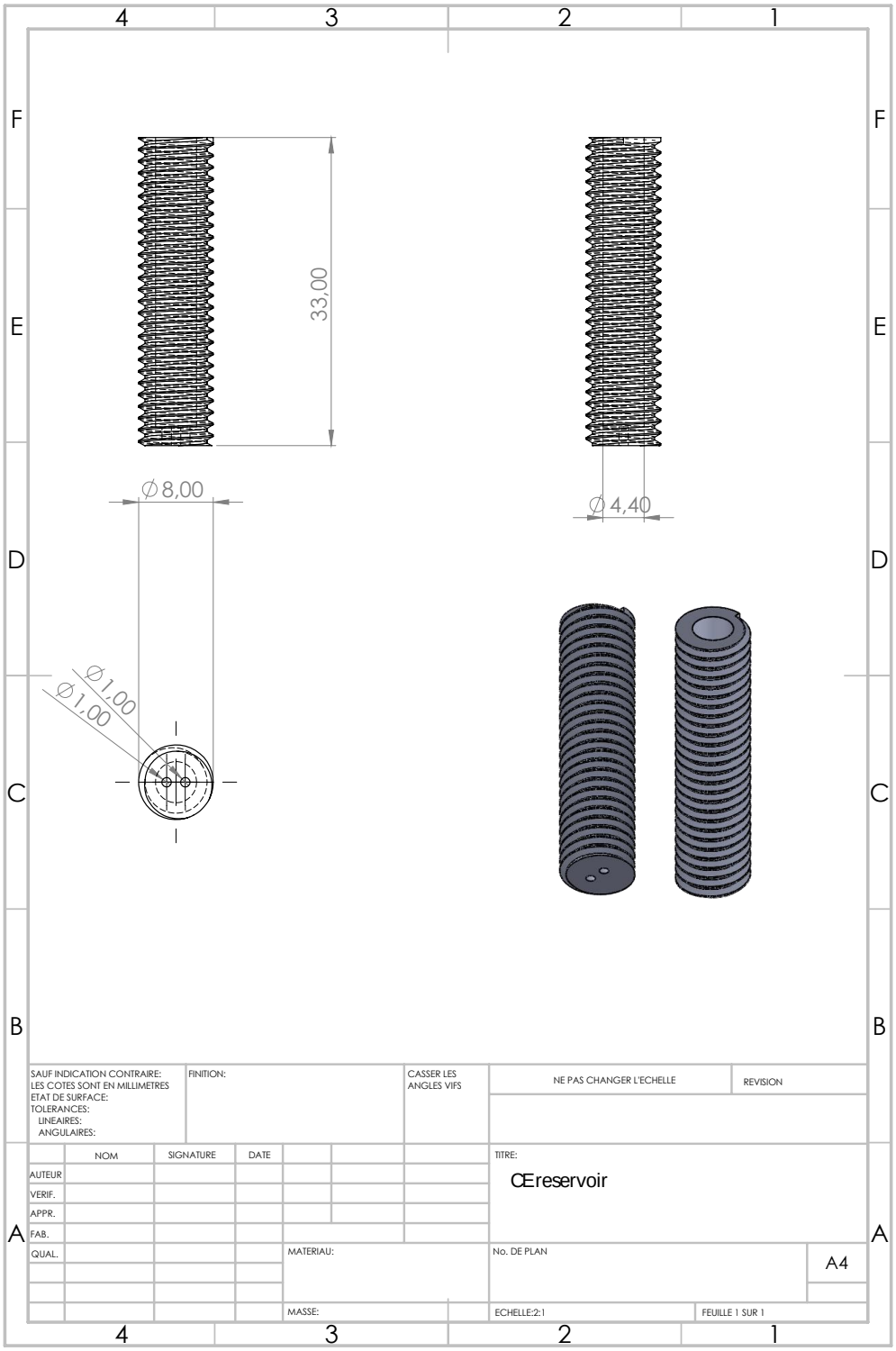


Figure S6. Drawing of the counter-electrode reservoir, to be inserted to the top part of the mini redox-flow battery. The Nafion membrane is stuck between these two pieces. The dimensions are in millimeters.

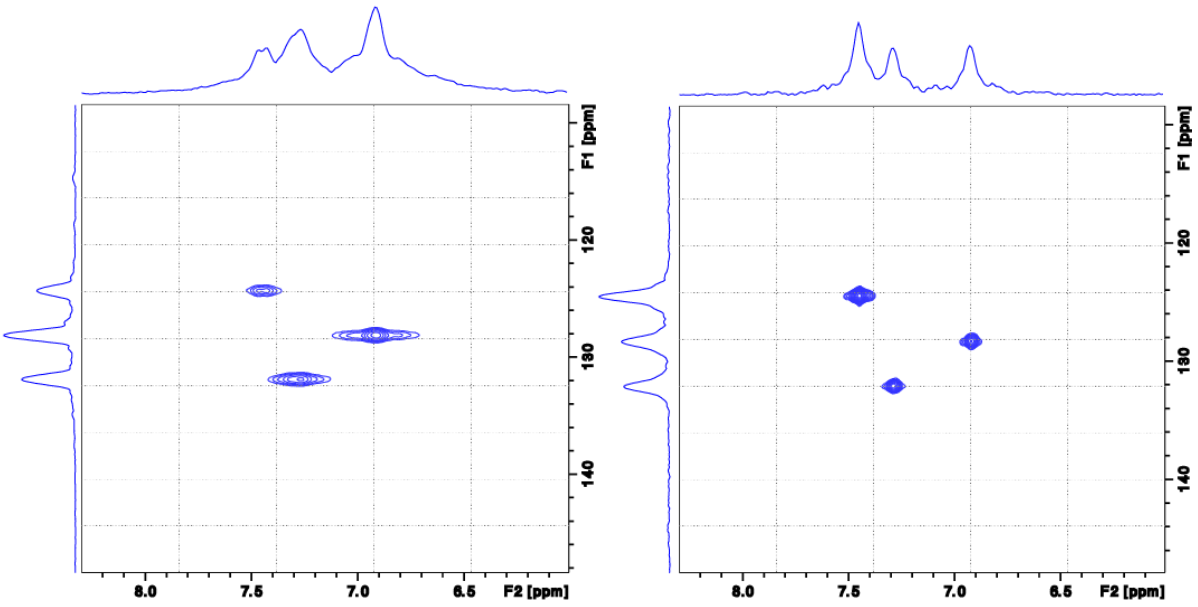


Figure S7. Comparison between classical ^{1}H-^{13}C HSQC (left) and spatially-localized ^{1}H-^{13}C HSQC (right) performed on 2,7-AQDS. 0.5 M. Both experiments have been performed with the same experimental conditions (10 ppm, 1024 complex points in the ^{1}H dimension; 40 ppm, 128 points in the ^{13}C dimension; 32 scans, for 1h17 experiment time). Also the processing is the same: apodization by a sine bell shifted by $\pi/2.5$ in both dimensions and zero-filling to 512 points in the ^{13}C dimension.

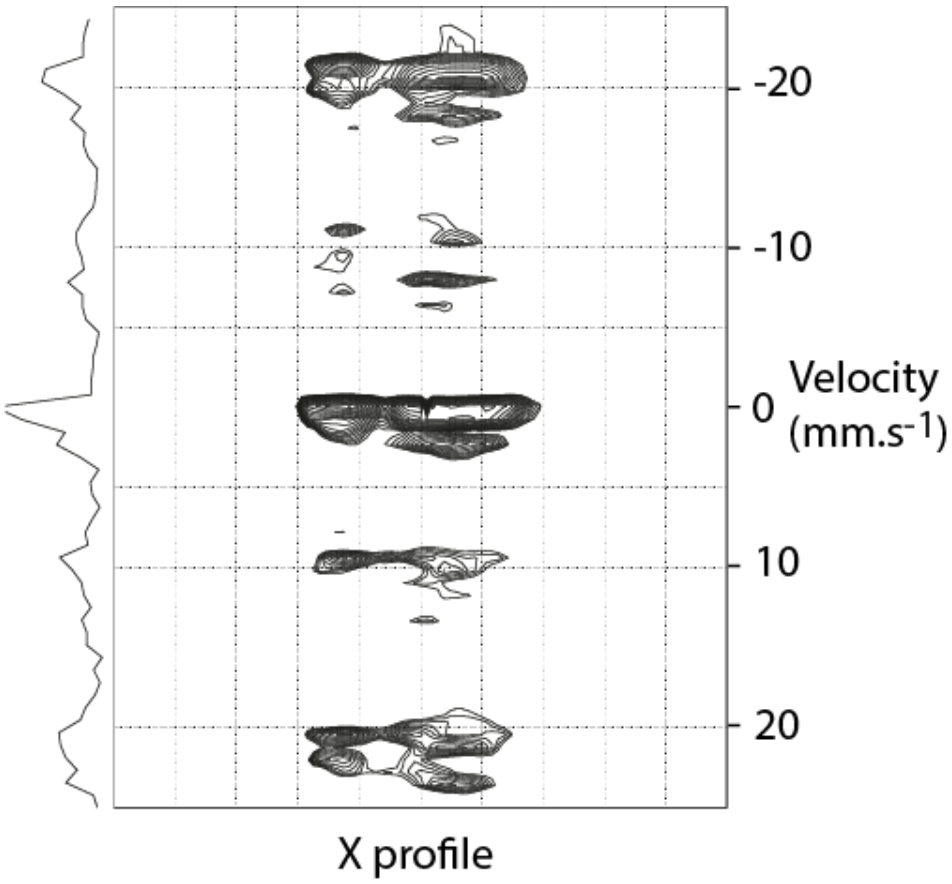


Figure S8. NMR velocimetry experiment performed with insufficient solution level inside the upper part of the insert. Signals on both sides of the zero frequency in the indirect dimension indicate that the solution oscillates but does not experience a net displacement.

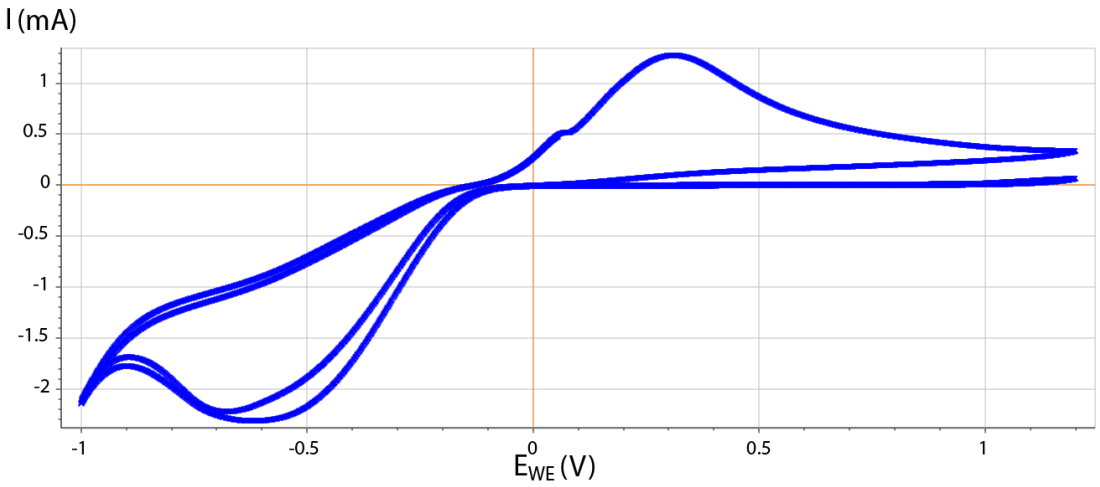
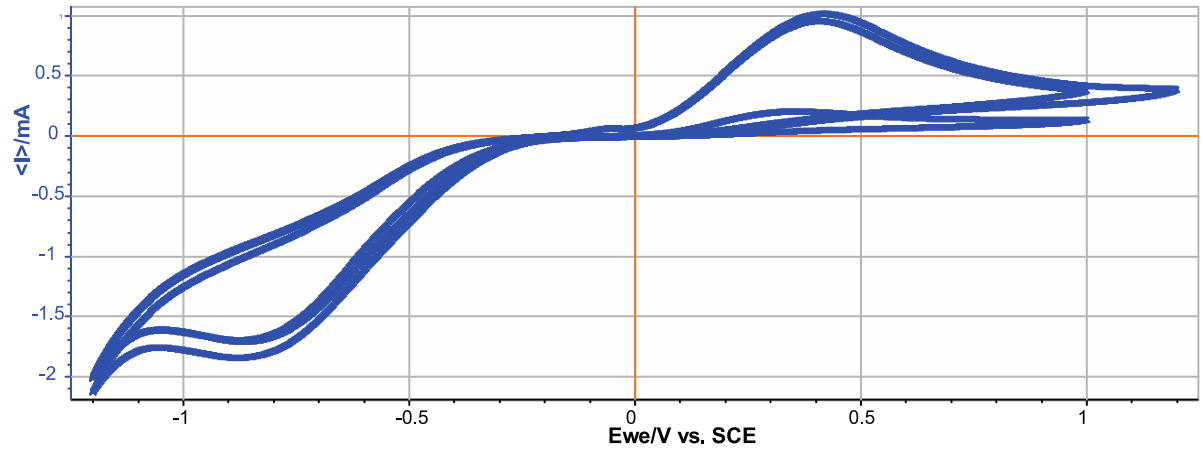


Figure S9. Cyclic Voltammetry recorded on the cell filled with oxidized 2,7-AQDS 50 mM in H_2SO_4 0.2 M (without solution flow). Scan rate 50 mV/s from +1.2 V to -1 V with 2 loops.

a)



b)

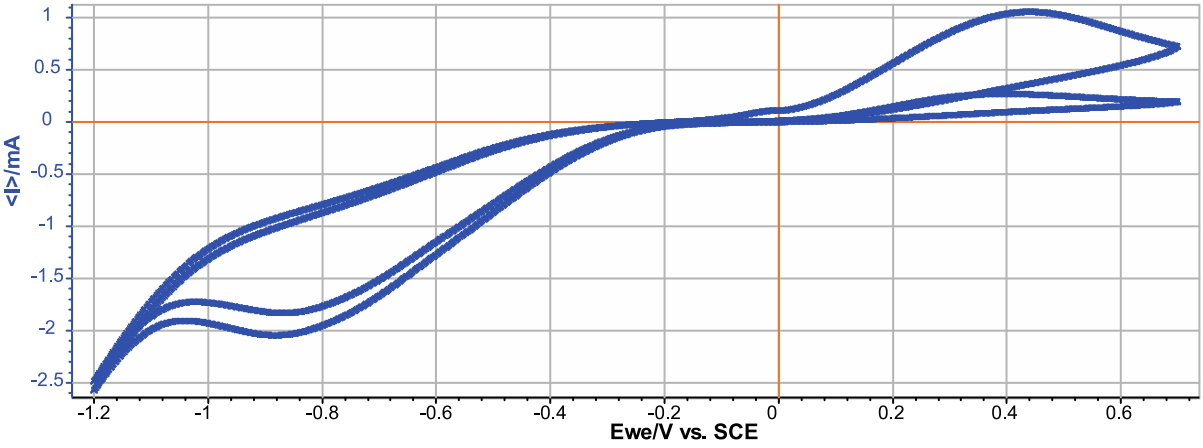


Figure S10. Influence of the magneto-hydrodynamic effect on the cyclic voltammetry. a) cell in a magnetic field lower than 5 gauss; b) cell placed inside the 11.7 T magnet. 2,7-AQDS 50 mM in H_2SO_4 0.2 M without solution flow, scan rate 50 mV/s.

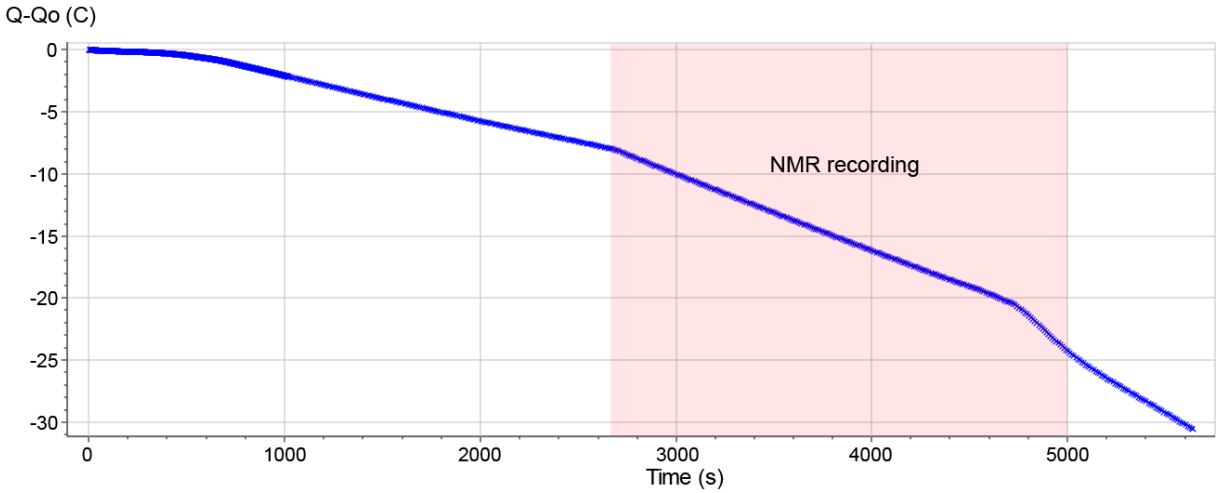


Figure S11. Chronoamperometry performed on the cell filled with oxidized 2,7-AQDS 50 mM in H_2SO_4 0.5 M (with solution flow). The time period in which the ^1H spectra have been recorded is represented by a pink area. The respective voltages applied are -0.3 V until the NMR starts (without effect on the anthraquinone; the first 1H NMR spectra still show the oxidized form) and -0.5 V after.

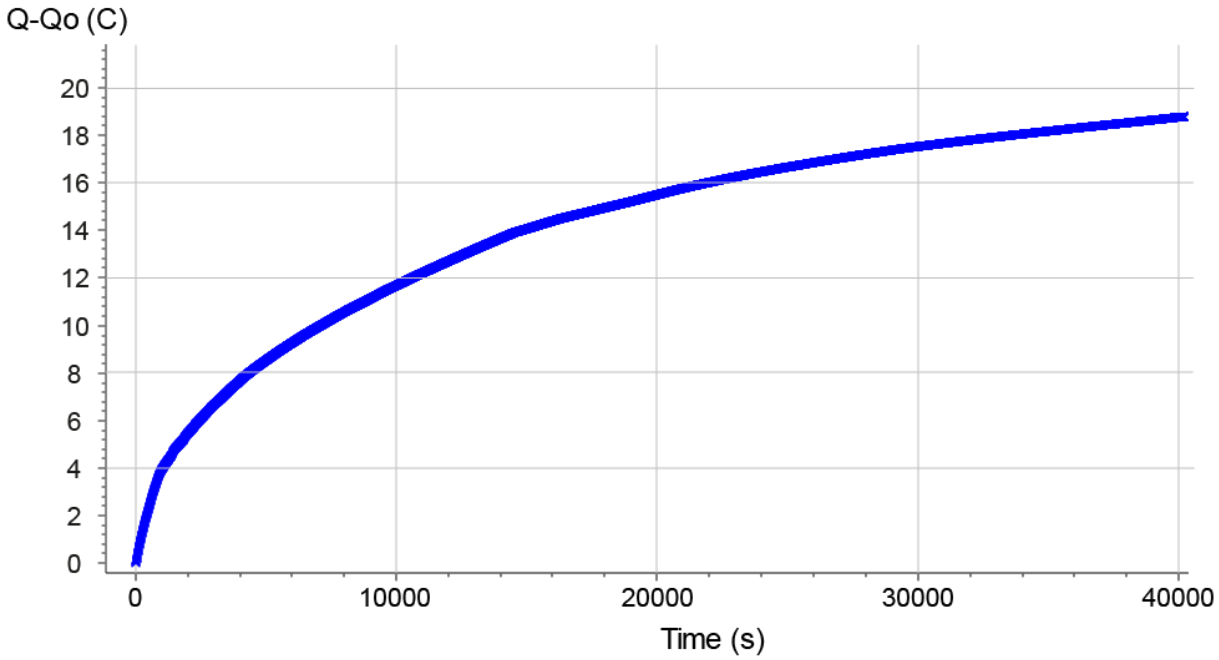


Figure S12. Chronoamperometry performed on the cell filled with reduced 2,7-AQDS 50 mM in H_2SO_4 0.5 M (with solution flow). A voltage of +0.45 V is applied.

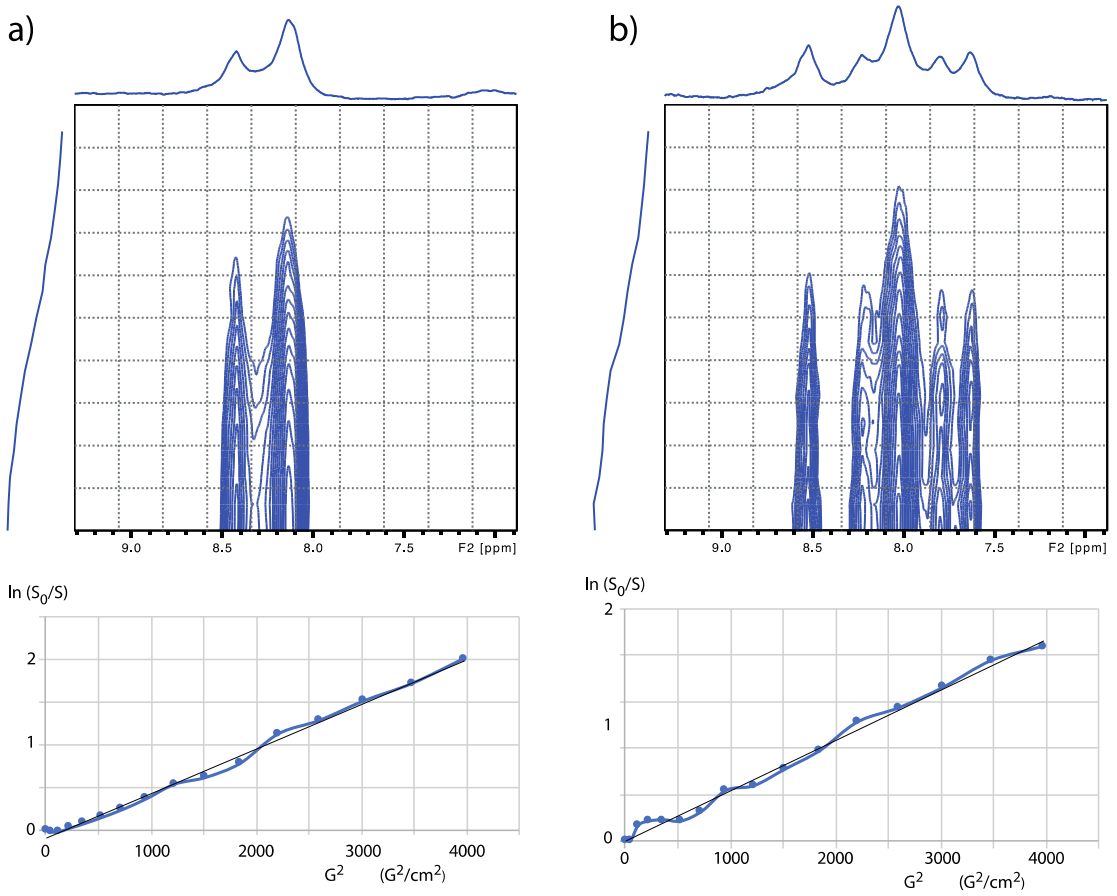


Figure S13. 2D DOSY experiments performed on a) the oxidized state of AQDS, b) the intermediate state where six ^{1}H signals appear. At the bottom the curves $\ln(S_0/S) = f(G^2)$ that have enabled extraction of the diffusion coefficients (S_0 is the signal recorded with the lowest gradient value of 2.8 G/cm) are displayed. Note that the sum of all the aromatic proton signals has been used.